GEOPHYSICS

Superionicity of oxygen-deficient davemaoite and its impact on the deep-Earth oxidation cycle

Zifan Wang[1], Yu He[1,2], Ho-kwang Mao[1,3], Duck Young Kim[1,3]*

Davemaoite ($CaSiO_3$ perovskite) is an essential mineral in Earth's lower mantle, thought to be solidified directly from an early magma ocean. Despite its abundance, the impact of defects, particularly oxygen vacancies, on davemaoite's properties under mantle conditions has not been thoroughly investigated. Here, we use machine learning molecular dynamic simulations to examine the behavior of oxygen-deficient davemaoite structures under high pressures and temperatures. Our simulations reveal its superionic transition driven by oxygen's diffusion, enhancing electrical conductivities. Our predicted phase diagrams demonstrate that higher oxygen vacancy concentrations expand the superionic phase region. This superionic behavior implies that defective davemaoite could play a critical role in early mantle oxidation and deep-Earth oxygen cycling, providing a potential major source of mobile oxygen in the deep mantle. These findings offer fresh insights into the geodynamic processes in Earth's early mantle and suggest that oxygen-deficient davemaoite could primarily contribute to the electrical conductivity and oxidation state of the deep lower mantle.

INTRODUCTION

Davemaoite, a $CaSiO_3$ perovskite, is the third most abundant mineral in Earth's lower mantle. First identified in a diamond inclusion from Orapa in Botswana, this rare perovskite sample was named "davemaoite" in honor of geoscientist Dave (Ho-kwang) Mao for his remarkable contributions to high-pressure geophysics and petrology (*1*). As $CaSiO_3$ perovskite, davemaoite is stable across a wide range of pressures and temperatures in the lower mantle, influencing many essential geophysical properties of Earth's interior (*2*–*5*). In addition, $CaSiO_3$ perovskite can host large amounts of incompatible elements like Al, Ti, and rare earth elements, playing a crucial role in Earth's geochemical evolution (*6*, *7*).

In Earth's interior, $CaSiO_3$ undergoes a series of transformations. Under ambient conditions, $CaSiO_3$ exists as wollastonite, which transitions to breyite at ~3 GPa (*8*) and further dissociates to Ca_2SiO_4 larnite and $CaSi_2O_5$ titanite at ~10 GPa (*9*). At ~15 GPa, Ca_2SiO_4 larnite and $CaSi_2O_5$ titanite recombine to form $CaSiO_3$ perovskite (*9*–*12*). With increasing temperature, $CaSiO_3$ perovskite transitions from a tetragonal (I4/mcm) phase to a stable cubic (Pm-3m) phase, known as davemaoite (*13*–*15*). Because of its importance as one of indicative minerals at lower mantle, various theoretical and experimental studies have explored the physical properties of davemaoite, revealing its stability (*16*, *17*), low seismic wave speeds (*4*, *18*), high thermal conductivity (*19*), weak rheological strength (*20*), and high melting temperatures (*21*).

Defects in Earth's minerals, categorized as point, line, planar, and bulk defects, are widespread and play crucial roles in geological processes. These defects, including misplaced atomic impurities, shifted atomic planes, and foreign inclusions, form naturally through mechanisms such as crystal growth, self-irradiation, radioactive isotope decay, and water-rock interactions. Defective minerals, such as silicates, kaolinites, and zeolites, are important as potential hydrogen storage or carbon sources within Earth's interior (*22*–*27*). Studies have highlighted the effects of defect type, size, and concentration on mineral properties, revealing their impact on adsorption, stability, and consequently mantle evolution (*28*–*31*).

Oxygen defects, in particular, have a pronounced impact on perovskites. In materials science, oxygen defects are known to increase ionic conductivity in perovskite materials. For example, Wang *et al.* (*32*) found that oxygen-deficient strontium cobalt oxide ($SrCoO_{2.5}$) exhibits enhanced ionic conductivity through oxygen diffusion at high pressures. Similarly, we hypothesize that analogous behaviors might occur in perovskite minerals within Earth's interior. Wall and Price (*33*) observed that oxygen-deficient $MgSiO_{2.5}$ perovskite minerals exhibit high conductivity (~100 S/m) under lower mantle conditions through molecular dynamic simulations. Wright and Price (*34*) reported similar findings in oxygen-deficient $SrTiO_3$ and $CaTiO_3$. However, there has been limited investigation into the defects and effects on other dominant lower-mantle perovskites. As an essential lower mantle perovskite, davemaoite is a promising candidate to study oxygen defect concentrations and behaviors under extreme conditions. The diffusive behavior of defective davemaoite at high temperatures may provide insights into the early magma ocean and the Hadean Earth's mantle.

In this study, we present computational simulation results for oxygen-deficient davemaoite. We generated four oxygen-deficient davemaoite structures: $CaSiO_{2.96}$, $CaSiO_{2.875}$, $CaSiO_{2.75}$, and $CaSiO_{2.5}$. Machine learning molecular dynamic (MLMD) simulations reveal a superionic behavior with oxygen diffusion in these minerals under extreme conditions, resulting in high diffusion coefficients and electrical conductivities. We propose that these diffusive, superionic O^{2-} may contribute to early mantle oxidation and the oxygen cycle in the deep Earth.

RESULTS

Superionic behavior

We designed a series of oxygen-deficient davemaoite structures with varying oxygen vacancy concentrations: $CaSiO_{2.96}$, $CaSiO_{2.875}$,

[1]Center for High Pressure Science and Technology Advanced Research (HPSTAR), Shanghai 201203, P.R. China. [2]Key Laboratory of High-Temperature and High-Pressure Study of the Earth's Interior, Institute of Geochemistry, Chinese Academy of Sciences, Guiyang 550081, Guizhou, P.R. China. [3]Shanghai Key Laboratory of Material Frontiers Research in Extreme Environments (MFree), Institute for Shanghai Advanced Research in Physical Sciences (SHARPS), Shanghai 201203, P.R. China.
*Corresponding author. Email: duckyoung.kim@hpstar.ac.cn

$CaSiO_{2.75}$, and $CaSiO_{2.5}$. We created several supercells of stoichiometric $CaSiO_3$ crystal structures and introduced oxygen defects. These defected structures were configured to achieve specific oxygen concentration: $CaSiO_{2.96}$, $CaSiO_{2.875}$, $CaSiO_{2.75}$, and $CaSiO_{2.5}$, represented by supercells $Ca_{27}Si_{27}O_{80}$, $Ca_{32}Si_{32}O_{92}$, $Ca_{32}Si_{32}O_{88}$, and $Ca_{36}Si_{36}O_{90}$, respectively (Fig. 1). Electron localization function (ELF) calculations revealed that all these structures are electrides, with interstitial anionic electrons occupying the oxygen vacancies (fig. S1). With temperature increasing, numerous studies on various perovskites materials demonstrated that more oxygen atoms tend to diffuse and leave their equilibrium positions, leading to higher oxygen vacancies (*35*–*38*). Similarly, davemaoite could easily loose oxygen atoms at high pressure and temperature conditions inside Earth, resulting in the deficient structures.

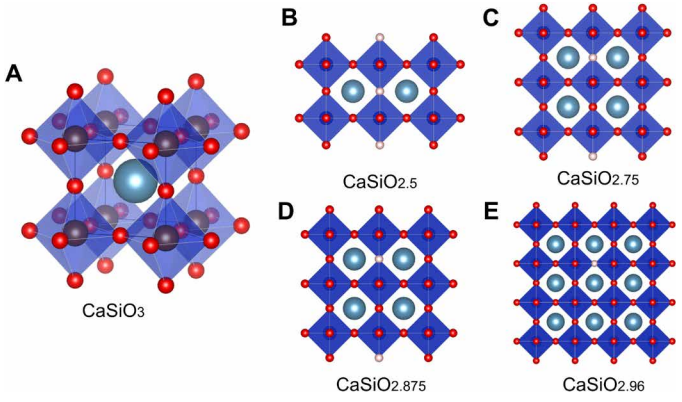

Fig. 1. The structures of perfect davemaoite and oxygen-deficient davemaoites. (**A**) $CaSiO_3$. (**B**) $CaSiO_{2.5}$. (**C**) $CaSiO_{2.75}$. (**D**) $CaSiO_{2.875}$. (**E**) $CaSiO_{2.96}$. The blue, brown, red, and white spheres represent Ca atoms, Si atoms, O atoms, and oxygen vacancies, respectively.

To investigate the dynamical properties of these oxygen-deficient davemaoite structures under early Earth's mantle conditions, we conducted MLMD simulations across a range of extreme pressures and temperatures. Using machine learning force field (MLFF) potentials, trained with ab initio molecular dynamic (AIMD) data at various pressures and temperatures, allowed us to perform simulations over long-enough timescales and with large supercells—both of which would be impractical with AIMD simulations alone. The MLMD simulations provided a reliable method for identifying the diffusive and melting behaviors of these structures over extended simulation times and large systems. In this study, we performed MLMD simulations with supercells containing ~1000 atoms for up to 100 ps.

Our simulations revealed superionic behavior in these oxygen-deficient davemaoite structures under high pressures and temperatures. This behavior is characterized by diffusive oxygen atoms in a stable lattice of Ca and Si atoms. Superionic behavior, which exhibits both solid and liquid characteristics, is discovered in light-element bearing compounds under extreme pressures and temperatures, especially in Earth and giant planets (*39*–*47*). Figures 2 (A to C) and 3 (D to F) illustrate the superionic behavior observed in these structures, represented by the average mean squared displacement (MSD) and trajectory snapshots in NVT (N, number of atoms; V, volume; T, temperature) ensembles. At lower temperatures, atoms oscillate around their equilibrium positions, maintaining typical solid structure. As temperatures rise into the superionic region, oxygen atoms leave their equilibrium positions and diffuse freely like liquid, while Ca and Si atoms remain within harmonic potentials. The MSD values of oxygen increase linearly with time, indicating nonzero diffusion coefficients for oxygen ($D_O > 0$), while Ca and Si remain stable ($D_{Ca,Si} = 0$). At even higher temperatures, the entire structure melts as all atoms begin to diffuse.

Further analysis confirmed the dynamical stability of the oxygen-deficient davemaoite structures. Phonon calculations indicated

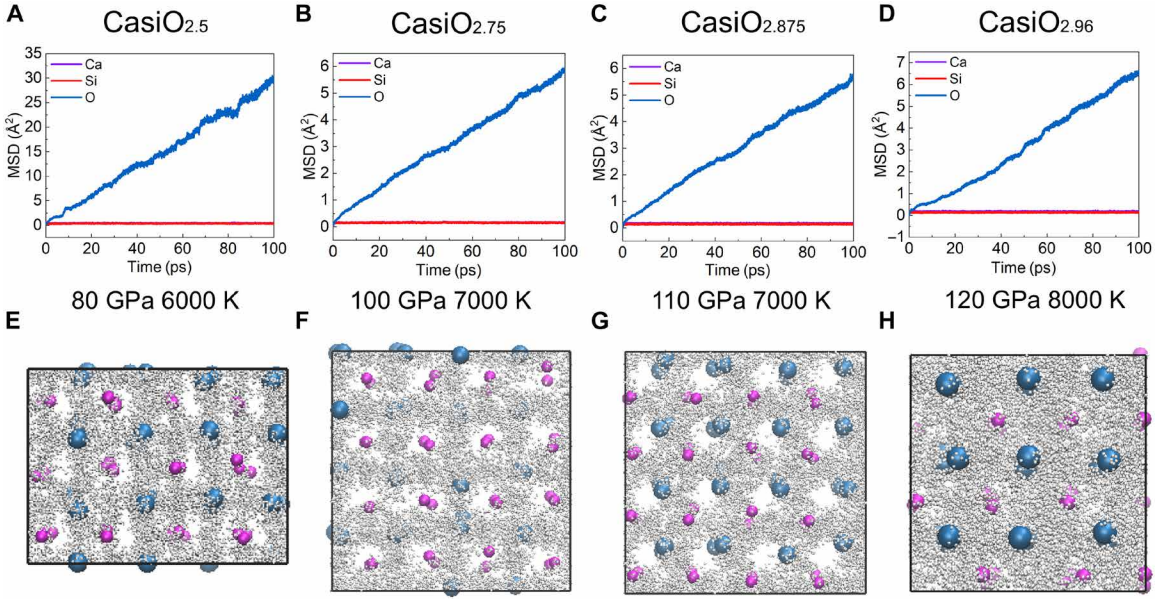

Fig. 2. Dynamical behaviors of oxygen-deficient davemaoite structures at extreme conditions. (**A** to **D**) The MSD of $CaSiO_{2.5}$ (A), $CaSiO_{2.75}$ (B), $CaSiO_{2.875}$ (C), and $CaSiO_{2.96}$ (D) under superionic regions. (**E** to **H**) The corresponding snapshots of MLMD trajectories in superionic states. In the snapshots of MLMD trajectories, the magenta, blue, and white spheres represent Ca, Si, and O atoms respectively.

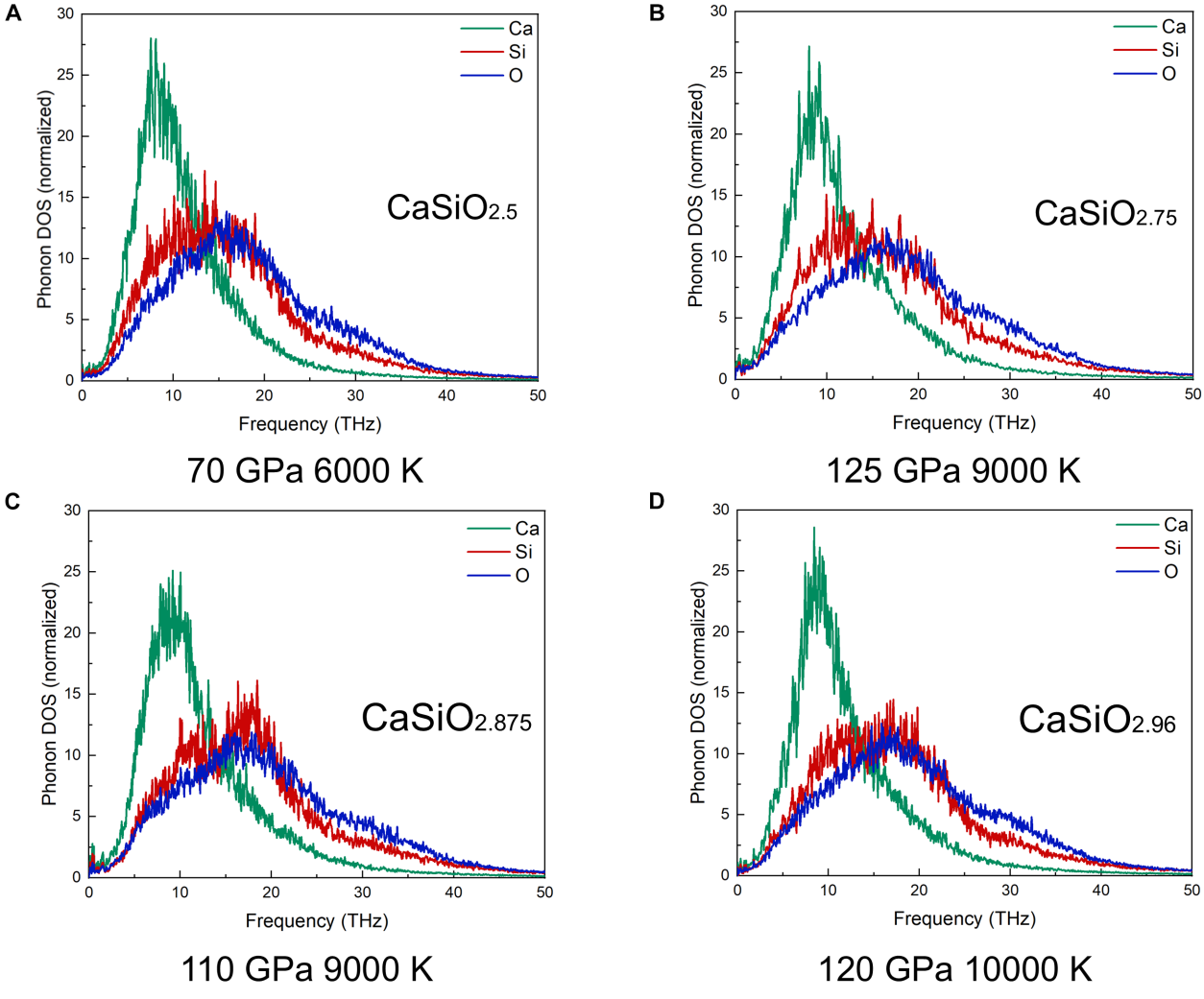

Fig. 3. Normalized phonon DOS of oxygen-deficient davemaoite structures at superionic conditions. (**A**) $CaSiO_{2.5}$ at 70 GPa, 6000 K. (**B**) $CaSiO_{2.75}$ at 125 GPa, 9000 K. (**C**) $CaSiO_{2.875}$ at 110 GPa, 9000 K. (**D**) $CaSiO_{2.96}$ at 120 GPa, 10000 K. The green, blue, and red lines represent Ca, Si, and O, respectively.

instability at low temperatures, while elevated temperatures stabilized the structures, as shown by consistent MSD values in MLMD simulations. We observed that the structures remain as a solid phase up to 1000 K, and the detailed temperature stability ranges are discussed further below. To validate stability in the superionic state, we calculated the phonon density of states (DOS) from MLMD trajectories within superionic regions (Fig. 3). Because of the extreme anharmonicity and partial occupancies in superionic phases, phonon spectra calculations are not feasible (*48*); however, the absence of imaginary frequencies in the phonon DOS confirmed the stability of superionic behavior in these oxygen-deficient davemaoite structures.

Phase diagram

To better understand the dynamical properties influenced by oxygen vacancies, we constructed P-T phase diagrams for two representative configurations: $CaSiO_{2.5}$ and $CaSiO_{2.96}$ (Fig. 4). These configurations represent the maximum and minimum oxygen vacancy concentrations in our study. The phase diagrams show solid, superionic, and liquid regions, providing insights into the behavior of each structure under specific pressure and temperature conditions. The modern geotherm and early Earth geotherm are represented by purple solid lines (*49*–*51*), which demonstrates that the superionic region of $CaSiO_{2.96}$ and $CaSiO_{2.5}$ cover the early Earth geotherm lines. We also estimated the melting temperature of $CaSiO_{2.5}$ using the two-phase method (*52*) to avoid superheating artifacts, represented by the black star symbol.

Oxygen vacancy concentration substantially affects the dynamical behavior of these structures at high pressures and temperatures. As shown in Fig. 4, $CaSiO_{2.5}$, with higher oxygen vacancy concentration, has a broader superionic region than $CaSiO_{2.96}$. The increased vacancy concentration in $CaSiO_{2.5}$ creates additional channels for oxygen diffusion, facilitating superionic behavior. Consequently, $CaSiO_{2.5}$ shows lower transition temperatures from solid to superionic and from superionic to liquid states compared to $CaSiO_{2.96}$. In structures with more vacancies, oxygen diffusion occurs at relatively low temperatures. Conversely, $CaSiO_{2.96}$ has a narrower and higher-temperature superionic region, displaying superionic behavior only at extreme temperatures around 3000 K higher than $CaSiO_{2.5}$ and persisting up to nearly 10,000 K.

Yin *et al.* (*21*) recently reported exceptionally high melting temperatures for perfect davemaoite based on first-principles molecular

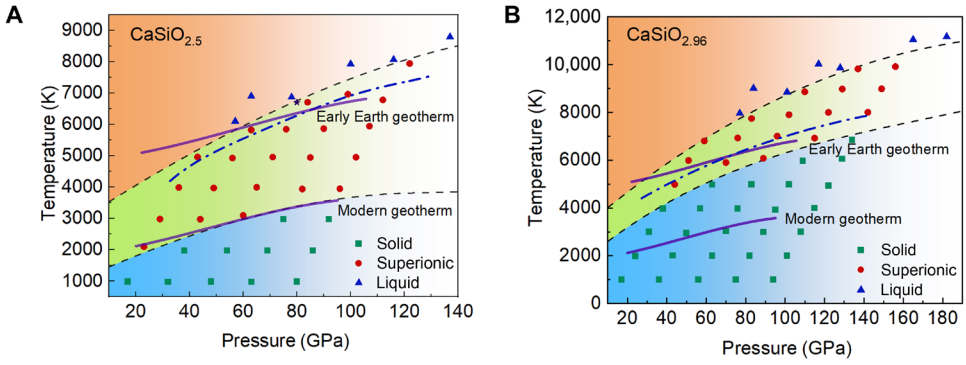

Fig. 4. Phase diagrams of oxygen-deficient davemaoite structures. (**A**) Phase diagram of $CaSiO_{2.5}$. (**B**) Phase diagram of $CaSiO_{2.96}$. The green squares, red circles, and blue triangles represent solid states, superionic states, and liquid states, respectively. The black star represents the melting temperature of $CaSiO_{2.5}$ determined by the two-phase method, ~6600 K at 70 GPa. The melting line of perfect davemaoite is represented by a dash-dotted line, according to the work of Yin *et al.* (*21*). The modern geotherm and early Earth geotherm are represented by purple solid lines, according to (*49*–*51*).

dynamic simulations. They predicted that davemaoite has the highest melting temperature among mantle minerals, reaching ~7700 K at ~136 GPa, with no superionic behavior observed in perfect crystals. Our MLMD simulations on perfect davemaoite under extreme conditions align with these findings, showing no superionic behavior (see fig. S2), confirming the solid stability at 110 GPa and 7000 K, indicative of high melting temperatures.

To compare with similar mantle minerals, we also simulated oxygen-deficient bridgmanite ($MgSiO_{2.5}$) under extreme conditions. As shown in fig. S3, $MgSiO_{2.5}$ exhibits superionic behavior but only within a narrow temperature range. Mg and Si sublattices in $MgSiO_{2.5}$ start melting with a slight increase of ~1000 K, transitioning the structure into a liquid state. We speculate that this difference is due to the smaller atomic size of Mg compared to Ca, making the Mg sublattice less stable under high temperatures. In contrast, Ca atoms form a robust sublattice within diffusive oxygen, making oxygen-deficient davemaoite unique among mantle minerals.

Oxygen defects considerably influence melting temperatures by inducing superionic states. This effect can be observed by comparing them with the melting lines of perfect davemaoite and bridgmanite, shown as blue dashed lines in Fig. 4 and fig. S3, respectively. Oxygen vacancies facilitate superionic transitions involving diffusive O^{2-}, which can be explained by the increased entropy, consequently raising the melting temperature. In Gibbs free energy ($G = H - TS$, where G is the Gibbs free energy, H is the enthalpy, T is the temperature, and S is the entropy), systems with higher entropy are more stable and require additional energy to transition to a fully liquid state. This phenomenon is commonly observed in the superionic phases of various materials, such as ice (*53*, *54*).

Diffusive O^{2-}

Superionic behaviors exhibit notable diffusion. We analyzed the diffusive behavior of oxygen in $CaSiO_{2.5}$ and $CaSiO_{2.96}$ in their superionic states to better understand this property. Diffusion coefficients for oxygen at various pressures and temperatures in these oxygen-deficient configurations were calculated on the basis of MLMD simulations (Fig. 5, A and B). The results indicate that oxygen diffusion increases with rising temperatures, marking the transition from solid to superionic and then to liquid. Notably, the diffusion coefficients for oxygen are about an order of magnitude lower than those of hydrogen in typical hydrous mantle minerals, consistent with the mass ratio of oxygen. Specifically, diffusion coefficients for oxygen (D_O) range from 0 to ~5×10^{-10} m^2/s in the superionic state of $CaSiO_{2.5}$ and from 0 to ~1.5×10^{-10} m^2/s in $CaSiO_{2.96}$. Higher vacancy concentrations in $CaSiO_{2.5}$ allow greater oxygen mobility, increasing diffusion.

In addition, we calculated the electrical conductivity of superionic $CaSiO_{2.5}$ and $CaSiO_{2.96}$ from MLMD results using the Nernst-Einstein equation. Figure 5 (C and D) shows the electrical conductivity for $CaSiO_{2.5}$ and $CaSiO_{2.96}$ under various pressures and temperatures, respectively. Consistent with diffusion coefficients, $CaSiO_{2.5}$ exhibits higher conductivity values than $CaSiO_{2.96}$, with conductivities (σ) ranging from ~2 to ~34 S/m in the superionic state of $CaSiO_{2.5}$ and ~1.3 to ~8 S/m in $CaSiO_{2.96}$. Upon melting, conductivity reaches ~200 S/m for $CaSiO_{2.5}$ and ~300 S/m for $CaSiO_{2.96}$ near their respective melting points. The total conductivity, σ_{tot}, increases to approximately 10^3 S/m in the fully liquid state.

Our calculated diffusion coefficients for oxygen (~10^{-10} m^2/s) are notably high compared with other minerals in the deep lower mantle (*55*–*59*), approaching the fastest diffusion limits and resulting in high ionic conductivities. Accordingly, the diffusion length (L) over time can be estimated using $L = 2\sqrt{Dt}$, where D is the diffusion coefficient and t is the time. For davemaoite, the diffusion length is predicted to be ~8 km over 1 billion years. While this distance is small and unlikely to greatly alter the structure of the lower mantle, it may strongly influence chemical reactions at boundary layers, such as the core-mantle boundary, large low–shear velocity provinces, and subduction zones.

Beyond seld-diffusion, O^{2-} transport can be enhanced by chemical potential gradients arising from redox state variation across phases. In addition, ionic diffusion under electromagnetic fields can be anisotropic, with rates up to an order of magnitude higher in specific directions (*60*, *61*). Such external fields could promote O^{2-} transport and chemical reactions in the lower mantle, particularly at boundary layers.

DISCUSSION

Davemaoite is thought to have solidified from the early magma ocean due to its high melting temperature, forming a solid $CaSiO_3$ layer above Earth's liquid core (*21*). This insulating layer was believed

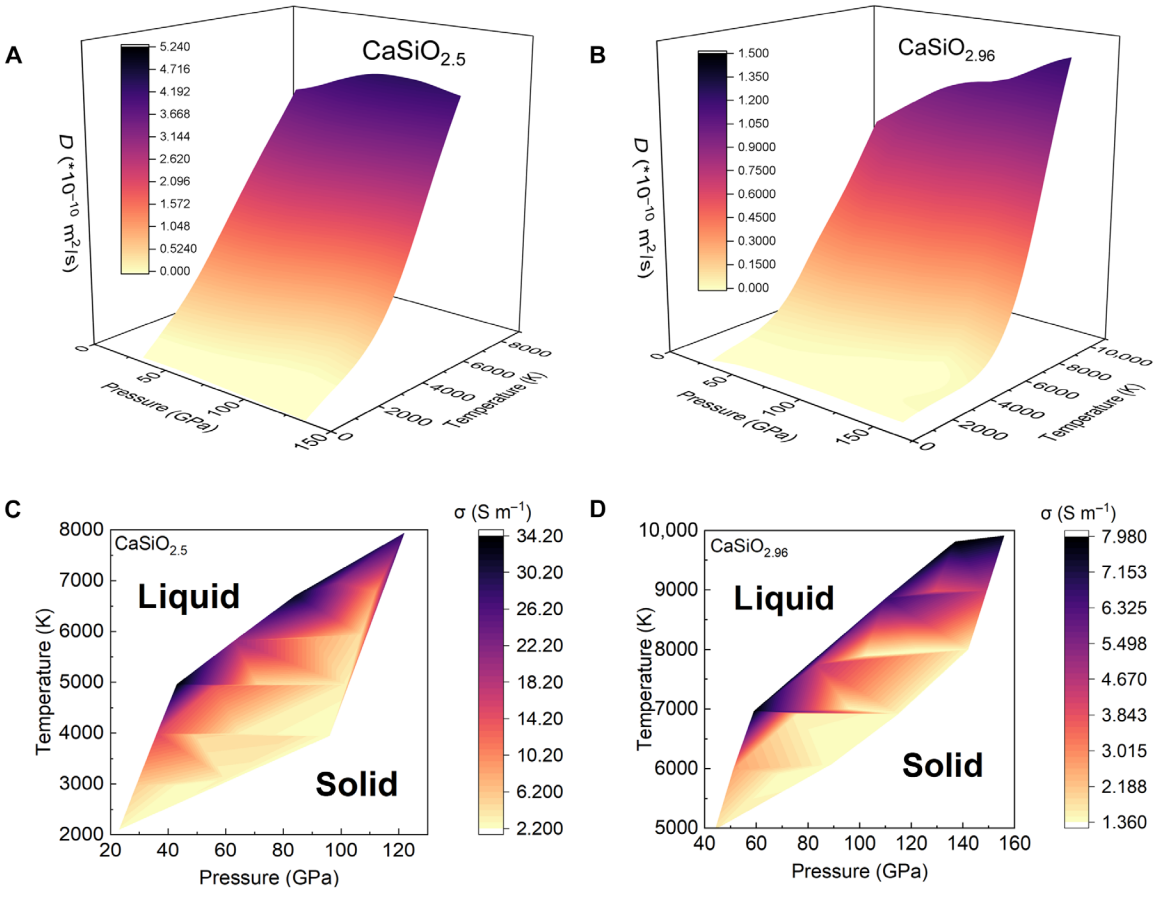

Fig. 5. Diffusive properties of oxygen-deficient davemaoite structures. (**A** and **C**) Diffusive properties of $CaSiO_{2.5}$. (**B** and **D**) Diffusive properties of $CaSiO_{2.96}$. (A) and (B) The diffusion coefficients of oxygen in solid and superionic states. (C) and (D) The electrical conductivities of oxygen in superionic states.

to help retain high temperatures within the core and contribute to the low-velocity zone in the deep lower mantle due to its slow seismic wave velocities. However, our findings reveal that this $CaSiO_3$ layer may not be entirely solid in the presence of oxygen-deficient davemaoite at high temperatures. In this layer, oxygen vacancies can lead to the formation of diffusive O^{2-} under the early magma ocean conditions. These defects naturally form in perovskites at high-temperature conditions (*34*–*37*) and are geologically widespread due to irradiation from radioactive isotopes and interactions with magma ocean elements (*62*). Experimental studies also confirm that oxygen defects in $CaSiO_3$ are associated with the incorporation of Fe^{3+} and Al^{3+} (*63*–*65*). During Earth's early history, the high availability of Fe^{3+} and Al^{3+} likely enhanced defect generation in $CaSiO_3$, making oxygen defects a common feature in davemaoite.

The presence of diffusive O^{2-} enhances the electrical conductivity of the $CaSiO_3$ layer, indicating that this layer may be at least partially conductive. Given that the davemaoite layer constitutes an integral part of the lower mantle, these high electrical conductivities could be sustained at great depths. Over the past decades, numerous studies have examined electrical conductivities in the lower mantle, particularly focusing on perovskite minerals. Many compositions of $(Mg, Fe)(Al, Si)O_3$ minerals have been shown to exhibit high conductivities, enhancing geomagnetic data interpretation (*66*–*69*). Notably, Fei *et al.* (*69*) reported electrical conductivities below 5 S/m for $CaSiO_3$ perovskite at pressures of 17 to 24 GPa and temperatures of 1300 to 2000 K, relevant to the uppermost lower mantle. Stixrude *et al.* (*70*) also reported that hot silicate liquids can exhibit electrical conductivities exceeding 10,000 S/m under basal magma ocean conditions. However, because of experimental limitations, measuring the conductivity of perovskites at the base of the lower mantle and near the core-mantle boundary remains challenging. Our simulations offer valuable references for the conductivity of perovskite minerals under such extreme conditions.

Diffusive O^{2-} may also play a critical role in early mantle oxidation. The Hadean mantle is thought to have been highly reducing during core-mantle differentiation from the magma ocean, before the core and mantle fully formed. To explain the great oxidated mantle, researchers have proposed a redox disproportionation mechanism, where ferrous iron (Fe^{2+}) converts to ferric iron (Fe^{3+}) and metallic iron (Fe^0) within a magma ocean. In this model, metallic iron segregates to the core, leaving an increasingly oxidized upper mantle. Armstrong *et al.* (*71*) demonstrated that Fe^{2+} can disproportionate to Fe^{3+} and metallic iron under high pressures in andesitic melts, while Kuwahara *et al.* (*72*) observed similar results with high Fe^{3+} content in magma derived from peridotite melts. Previous studies have assumed that reacted fugacious oxygen originates directly from the magma ocean. Our findings suggest that diffusive O^{2-} could also escape from the davemaoite layer. The mobile O^{2-} in defective davemaoite likely participated in these oxidation reactions, producing oxygen-rich ferric iron and silicates, which contributed

to the oxidized mantle. Thus, these mobile O^{2-} could react with ferric iron or other mantle rocks, forming part of the oxidized mantle.

Furthermore, research by Hu *et al.* identified iron peroxides (FeO_2) at the high-pressure condition corresponding to the deep lower mantle, providing fresh insights into the oxygen cycle within Earth's interior (*73*–*75*). They suggested that oxygen-rich FeO_2 could act as a reservoir, forming a deep-Earth oxygen cycle and potentially triggering the Great Oxidation Event (GOE). The formation of FeO_2 requires an ample supply of oxygen, which oxygen-deficient davemaoite could provide. FeO_2 is expected to form in the deep lower mantle, where superionicity in defected davemaoite could serve as a substantial source of oxygen.

In this study, the $CaSiO_3$ layer is assumed to have solidified from a silicate magma ocean in Headen, about 4.6 billion years ago, when the core-mantle differentiation has not been completed. We speculate that diffusive O^{2-} plays prominent contribution in early mantle oxidation, reacting with metallic iron and forming oxidized compounds such as FeO_2. The accumulation of FeO_2-bearing patches in the deep mantle could potentially establish a deep-Earth oxygen cycle and act as a potential trigger for the GOE. It is worth noting that the GOE happens during the transition period from the Archean to the Proterozoic, about 2.6 billion years ago, which is much later than the onset of superionicity of davemaoite.

MATERIALS AND METHODS

Ab initio calculations

The oxygen defects are introduced by creating several supercells of stoichiometric $CaSiO_3$ crystal structures and randomly removing one oxygen atom. Specifically, $CaSiO_{2.96}$, $CaSiO_{2.875}$, $CaSiO_{2.75}$, and $CaSiO_{2.5}$ are created by randomly removing one oxygen atom in $3 \times 3 \times 3$, $2 \times 2 \times 2$, $2 \times 2 \times 1$, and $2 \times 1 \times 1$ supercells of perfect $CaSiO_3$, respectively. Ab initio calculations are performed by Vienna ab initio simulation package (VASP) (*76*) package with the projector augmented wave method (*77*). We used the generalized gradient approximation of Perdew-Burke-Ernzerhof (*78*) for the exchange-correlation functional with the cutoff energy of 800 eV. We treat $3s^2 3p^6 4s^2$, $3s^2$, $3s^2 3p^2$, and $2s^2 2p^4$ electrons as valence electrons for Ca, Mg, Si, and O atoms, respectively. Monkhort-Pack *k*-point mesh (*79*) with a $9 \times 9 \times 9$ mesh was used for the structural optimization calculations to get enough convergence at each pressure values. A Gaussian smearing method was adopted to treat electron temperature. The AIMD simulations were conducted with NVT or NPT (N, number of atoms; V, volume; T, temperature) ensembles using the Langevin thermostat (*80*) implemented by VASP. We first conducted low-precision molecular dynamic simulations at 600 eV with Γ point and then correct to 800 eV with a refined $2 \times 2 \times 2$ K-mesh, both with total simulation times of 10 ps and timesteps of 1 fs. We used NVT ensembles to produce AIMD data for constructing P-T phase diagrams and analyze diffusive properties such as diffusion coefficients and electrical conductivities. NPT ensembles were mainly used to conduct a two-phase method, aiming to correctly determine the melting temperatures. We also performed several AIMD simulations using NPT ensembles at the same conditions of NVT simulations to cross-check the superionic properties. The supercells contain 152 atoms, 156 atoms, 152 atoms, 162 atoms, and 124 atoms for $CaSiO_{2.96}$, $CaSiO_{2.875}$, $CaSiO_{2.75}$, $CaSiO_{2.5}$, and $MgSiO_{2.5}$, respectively.

Machine learning molecular dynamics

The MLFF potentials were constructed using the Deep Potential for Molecular Dynamics (DeePMD) (*81*, *82*), in which a deep neural network is trained to learn and generate potentials using atomic coordinates, energies, and forces from AIMD simulations data. The machine learning potentials were used separately trained via AIMD data at each P-T condition. We used 8000 configurations for training and 2000 configurations for testing. Several key training parameters are as follows: We choose se_e2_a as a descriptor which is constructed by full relative coordinates, the cutoff radius is 6.0, the number of neurons in each hidden layer of the embedding net is 10, 20, and 40, the fitting nets are 100, 100, and 100, the desired learning rate is 3.5×10^{-8}, and the total training step is 10^6. The MLMD simulations were carried out using the Large-scale Atomic/Molecular Massively Parallel Simulator (LAMMPS) code (*83*) with the force field potentials generated by DeePMD, using periodic boundary conditions and a time step of 1 fs. By adopting the machine learning potentials trained by AIMD data, we used NVT ensembles to construct P-T phase diagrams and analyze diffusive properties such as diffusion coefficients and electrical conductivities. NPT ensembles were also mainly used to conduct a two-phase method using AIMD-trained potentials. We also performed several molecular dynamic simulations using NPT ensembles at the same conditions of NVT simulations to cross-check the superionic properties. Multiple independent simulations were run to estimate the errors of diffusion coefficients and electrical conductivities, resulting in estimated errors up to ~2%. The MLMD simulations comprised the supercells containing 1072 atoms, 1248 atoms, 1216 atoms, 1296 atoms, and 1072 atoms respectively, for $CaSiO_{2.96}$, $CaSiO_{2.875}$, $CaSiO_{2.75}$, $CaSiO_{2.5}$, and $MgSiO_{2.5}$ under various pressures and temperatures for long timescale of 100 ps in NVT and NPT ensembles. We also conducted MLMD simulations with larger sizes (up to 9984 atoms) and longer time periods (500 ps) for a convergency test of size and simulation time.

Diffusion coefficient

The MSD of the *j*th species $\left\langle u_j^2(t) \right\rangle$ at time *t* was estimated as

$$\left\langle u_j^2(t) \right\rangle = \frac{1}{N_j} \sum_{j=1}^{N_j} \left\langle | r_j(t) - r_j(0) |^2 \right\rangle \quad (1)$$

where $r_j(t)$ is the *j*th atom position at time *t*, and N_j is the total number of atoms of element *j* in the simulation cell. The isotropic diffusion coefficient (*D*) of the *j*th element was estimated as

$$D = \left\langle u_j^2(t) \right\rangle / 6t \quad (2)$$

Electrical conductivity

We used the Nernst-Einstein equation ($\sigma = DNq^2/k_B T$) to calculate electrical conductivity. In the equation, q is the carrier electric charge ($2e$ for oxygen), D is the carrier diffusion coefficient, N is the carrier density, and T is the temperature. All these values can be extracted from the AIMD or MLMD trajectories with NVT and NPT ensembles.

Two-phase method

In the two-phase method, we built the cell that consists of coexisting liquid and solid with a common interface. The initial two-phase systems

were obtained by freezing half of the cell and running NVT ensemble simulations at very high temperatures to melt the other half. Then, we performed molecular dynamic simulations in the NPT ensemble until the cell becomes homogeneous. If the final system is liquid, then the temperature is above the melting point; if it is solid, then the temperature is under the melting point. We conducted several simulations at a series of temperatures at fixed pressures until the temperature gap was sufficiently small. We also used MLFF potentials in the simulations, running with the supercells of ~1000 atoms with up to 100 ps.

Phonon DOS

The phonon DOS $g(E)$ was obtained by Fourier transformation of the velocity autocorrelation function as

$$g_j(E) = \int e^{\frac{iEt}{\hbar}} \frac{\langle v_j(t) * v_j(0) \rangle}{\langle v_j(0) * v_j(0) \rangle} dt \quad (3)$$

$$g(E) = \sum_j g_j(E) \quad (4)$$

where j refers to the atom, $g_j(E)$ is the partial phonon DOS of the jth atom, $v_j(t)$ is the velocity vector of the jth atom at time t, and the symbol $\langle \cdots \rangle$ indicates an ensemble average over atoms.

Supplementary Materials

This PDF file includes:

Figs. S1 to S13
Tables S1 to S3

REFERENCES AND NOTES

1. O. Tschauner, S. Huang, S. Yang, M. Humayun, W. Liu, S. N. Gilbert Corder, H. A. Bechtel, J. Tischler, G. R. Rossman, Discovery of davemaoite, $CaSiO_3$-perovskite, as a mineral from the lower mantle. *Science* **374**, 891–894 (2021).
2. S. E. Kesson, J. D. Fitz Gerald, J. M. G. Shelley, Mineral chemistry and density of subducted basaltic crust at lower-mantle pressures. *Nature* **372**, 767–769 (1994).
3. K. Hirose, N. Takafuji, N. Sata, Y. Ohishi, Phase transition and density of subducted MORB crust in the lower mantle. *Earth Planet. Sci. Lett.* **237**, 239–251 (2005).
4. S. Gréaux, T. Irifune, Y. Higo, Y. Tange, T. Arimoto, Z. Liu, A. Yamada, Sound velocity of $CaSiO_3$ perovskite suggests the presence of basaltic crust in the Earth's lower mantle. *Nature* **565**, 218–221 (2019).
5. W. Wang, Y. Xu, D. Sun, S. Ni, R. Wentzcovitch, Z. Wu, Velocity and density characteristics of subducted oceanic crust and the origin of lower-mantle heterogeneities. *Nat. Commun.* **11**, 64 (2020).
6. K. Hirose, N. Shimizu, W. V. Westrenen, Y. Fei, Trace element partitioning in Earth's lower mantle and implications for geochemical consequences of partial melting at the core–mantle boundary. *Phys. Earth Planet. Inter.* **146**, 249–260 (2004).
7. M. J. Walter, E. Nakamura, R. G. Trønnes, D. J. Frost, Experimental constraints on crystallization differentiation in a deep magma ocean. *Geochim. Cosmochim. Acta* **68**, 4267–4284 (2004).
8. W.-L. Huang, P. J. Wyllie, Melting and subsolidus phase relationships for $CaSiO_3$ to 35 kilobars pressure. *Am. Mineral.* **60**, 213–217 (1975).
9. T. Gasparik, K. Wolf, C. M. Smith, Experimental determination of phase relation in the $CaSiO_3$ system from 8 to 15 GPa. *Am. Mineral.* **79**, 1219–1222 (1994).
10. S.-H. Shim, T. S. Duffy, G. Shen, The stability and P–V–T equation of state of $CaSiO_3$ perovskite in the Earth's lower mantle. *J. Geophys. Res.* **105**, 25955–25968 (2000).
11. M. Akaogi, M. Yano, T. Tejima, M. Iijima, H. Kojitani, High-pressure transitions of diopside and wollastonite: Phase equilibria and thermochemistry of $CaMgSi_2O_6$, $CaSiO_3$ and $CaSi_2O_5$–$CaTiSiO_5$ system. *Phys. Earth Planet. Inter.* **143-144**, 145–156 (2004).
12. Y. Sueda, T. Irifune, A. Yamada, T. Inoue, X. Liu, K. Funakoshi, The phase boundary between $CaSiO_3$ perovskite and Ca_2SiO_4 + $CaSi_2O_5$ determined by in situ X-ray observations. *Geophys. Res. Lett.* **33**, L10307 (2006).
13. D. J. Adams, A. R. Oganov, Ab initio molecular dynamics study of $CaSiO_3$ perovskite at P–T conditions of Earth's lower mantle. *Phys. Rev. B.* **73**, 184106 (2006).
14. L. Stixrude, C. Lithgow-Bertelloni, B. Kiefer, P. Fumagalli, Phase stability and shear softening in $CaSiO_3$ perovskite at high pressure. *Phys. Rev. B.* **75**, 024108 (2007).
15. D. N. Sagatova, A. F. Shatskiy, N. E. Sagatov, K. D. Litasov, Phase relations in $CaSiO_3$ system up to 100 GPa and 2500 K. *Geochem. Int.* **59**, 791–800 (2021).
16. J. C. A. Prentice, R. Maezono, R. J. Needs, First-principles anharmonic vibrational study of the structure of calcium silicate perovskite under lower mantle conditions. *Phys. Rev. B* **99**, 064101 (2019).
17. Z. Zhang, R. M. Wentzcovitch, Ab Initio anharmonic thermodynamic properties of cubic $CaSiO_3$ Perovskite. *Phys. Rev. B* **103**, 10 (2021).
18. A. R. Thomson, W. A. Crichton, J. P. Brodholt, I. G. Wood, N. C. Siersch, J. M. R. Muir, D. P. Dobson, S. A. Hunt, Seismic velocities of $CaSiO_3$ perovskite can explain LLSVPs in Earth's lower mantle. *Nature* **572**, 643–647 (2019).
19. Z. Zhang, D.-B. Zhang, K. Onga, A. Hasegawa, K. Ohta, K. Hirose, R. M. Wentzcovitch, Thermal conductivity of $CaSiO_3$ perovskite at lower mantle conditions. *Phys. Rev. B.* **104**, 184101 (2021).
20. J. Immoor, L. Miyagi, H.-P. Liermann, S. Speziale, K. Schulze, J. Buchen, A. Kurnosov, H. Marquardt, Weak cubic $CaSiO_3$ perovskite in the Earth's mantle. *Nature* **603**, 276–279 (2022).
21. K. Yin, A. B. Belonoshko, Y. Li, X. Lu, Davemaoite as the mantle mineral with the highest melting temperature. *Sci. Adv.* **9**, eadj2660 (2023).
22. B. E. Hobbs, The influence of metamorphic environment upon the deformation of minerals. *Tectonophysics* **78**, 335–383 (1981).
23. E. Libowitzky, A. Beran, OH defects in forsterite. *Phys. Chem. Minerals* **22**, 387–392 (1995).
24. K. Wright, Atomistic models of OH defects in nominally anhydrous minerals. *Rev. Mineral. Geochem.* **62**, 67–83 (2006).
25. J. C. Nisar, C. Arhammar, E. Jamstorp, R. Ahuja, Optical gap and native point defects in kaolinite studied by the GGA-PBE, HSE functional, and GW approaches. *Phys. Rev. B* **84**, 075120 (2011).
26. J. Wu, P. R. Buseck, Carbon storage at defect sites in mantle mineral analogues. *Nat. Geosci.* **6**, 875–878 (2013).
27. X. Li, H. Li, G. Yang, Promoting the adsorption of metal ions on kaolinite by defect sites: A molecular dynamics study. *Sci. Rep.* **5**, 14377 (2015).
28. B. E. Hobbs, Point defect chemistry of minerals under a hydrothermal environment. *J. Geophys. Res. Solid Earth* **89**, 4026–4038 (1984).
29. M. Konrad-Schmolke, R. Halama, R. Wirth, A. Thomen, N. Klitscher, L. Morales, A. Schreiber, D. H. Wilke Franziska, Mineral dissolution and reprecipitation mediated by an amorphous phase. *Nat. Commun.* **9**, 1637 (2018).
30. S. Demouchy, Defects in olivine. *Eur. J. Mineral.* **33**, 249–282 (2021).
31. V. V. Dobrosavljevic, D. Zhang, W. Sturhahn, S. Chariton, V. B. Prakapenka, J. Zhao, T. S. Toellner, O. S. Pardo, J. M. Jackson, Melting and defect transitions in FeO up to pressures of Earth's core-mantle boundary. *Nat. Commun.* **14**, 7336 (2023).
32. B. Wang, N. Li, Y. Zhao, X. Liu, M. Li, Q. Zhang, H. Dong, Y. He, D. Zhang, Y. Wang, G. Liu, Y. Long, W. Yang, A large enhancement of ionic conductivity in $SrCoO_{2.5}$ controlled by isostructural phase transition and negative linear compressibility. *Appl. Phys. Lett.* **119**, 043902 (2021).
33. A. Wall, G. D. Price, Electrical conductivity of the lower mantle: A molecular dynamics simulation of $MgSiO_3$ perovskite. *Phys. Earth Planet. Inter.* **58**, 192–204 (1989).
34. L. Wright, G. D. Price, Computer simulation of defects and diffusion in perovskites. *J. Geophys. Res. Solid Earth* **98**, 22245–22253 (1993).
35. L. Li, H. Yang, Z. Gao, Y. Zhang, F. Dong, G. Yang, M. Ni, Z. Lin, Nickel-substituted $Ba_{0.5}Sr_{0.5}Co_{0.8}Fe_{0.2}O_{3-\delta}$: A highly active perovskite oxygen electrode for reduced-temperature solid oxide fuel cells. *J. Mater. Chem. A* **7**, 12343–12349 (2019).
36. A. Bonkowski, C. Perkampus, R. A. De Souza, High oxygen-vacancy diffusivity predicted for perovskite oxide $Ca_{0.5}Sr_{0.5}Co_{0.8}Fe_{0.2}O_{2.5}$. *J. Mater. Chem. A* **11**, 10551–10555 (2023).
37. B. Baldassarri, J. He, C. Wolverton, Vibrational entropies of oxygen vacancy formation in metal oxides. *Phys. Rev. Mater.* **8**, 055407 (2024).
38. Z. Li, X. Mao, D. Feng, M. Li, X. Xu, Y. Luo, L. Zhuang, R. Lin, T. Zhu, F. Liang, Z. Huang, D. Liu, Z. Yan, A. Du, Z. Shao, Z. Zhu, Prediction of perovskite oxygen vacancies for oxygen electrocatalysis at different temperatures. *Nat. Commun.* **15**, 9318 (2024).
39. C. Cavazzoni, G. L. Chiarotti, S. Scandolo, E. Tosatti, M. Bernasconi, M. Parrinello, Superionic and metallic states of water and ammonia at giant planet conditions. *Science* **283**, 44–46 (1999).
40. M. Millot, F. Coppari, J. R. Rygg, A. C. Barrios, S. Hamel, D. C. Swift, J. H. Eggert, Nanosecond x-ray diffraction of shock-compressed superionic water ice. *Nature* **569**, 251–255 (2019).
41. C. Liu, H. Gao, Y. Wang, R. J. Needs, C. J. Pickard, J. Sun, H.-T. Wang, D. Xing, Multiple superionic states in helium–water compounds. *Nat. Phys.* **15**, 1065–1070 (2019).
42. P. Huang, H. Liu, J. Lv, Q. Li, C. Long, Y. Wang, C. Chen, R. J. Hemley, Y. Ma, Stability of H_3O at extreme conditions and implications for the magnetic fields of Uranus and Neptune. *Proc. Natl. Acad. Sci. U.S.A.* **117**, 5638–5643 (2020).
43. M. Hou, Y. He, B. G. Jang, S. Sun, Y. Zhuang, L. Deng, R. Tang, J. Chen, F. Ke, Y. Meng, V. B. Prakapenka, B. Chen, J. H. Shim, J. Liu, D. Y. Kim, Q. Hu, C. J. Pickard, R. J. Needs,

H.-K. Mao, Superionic iron oxide–hydroxide in Earth's deep mantle. *Nat. Geosci.* **14**, 174–178 (2021).
44. H.-F. Li, A. R. Oganov, H. Cui, X.-F. Zhou, X. Dong, H.-T. Wang, Ultrahigh-pressure magnesium hydrosilicates as reservoirs of water in early Earth. *Phys. Rev. Lett.* **128**, 035703 (2022).
45. Y. He, S. Sun, D. Y. Kim, B. G. Jang, H. Li, H. Mao, Superionic iron alloys and their seismic velocities in Earth's inner core. *Nature* **602**, 258–262 (2022).
46. S. Sun, Y. He, J. Yang, Y. Lin, J. Li, D. Y. Kim, H. Li, H. Mao, Superionic effect and anisotropic texture in Earth's inner core driven by geomagnetic field. *Nat. Commun.* **14**, 1656 (2023).
47. Y. He, D. Y. Kim, V. V. Struzhkin, Z. M. Geballe, V. Prakapenka, H. Mao, The stability of FeH_x and hydrogen transport at Earth's core mantle boundary. *Sci. Bull.* **68**, 1567–1573 (2023).
48. Q. Ren, M. K. Gupta, M. Jin, J. Ding, J. Wu, Z. Chen, S. Lin, O. Fabelo, J. A. Rodríguez-Velamazán, M. Kofu, K. Nakajima, M. Wolf, F. Zhu, J. Wang, Z. Cheng, G. Wang, X. Tong, Y. Pei, O. Delaire, J. Ma, Extreme phonon anharmonicity underpins superionic diffusion and ultralow thermal conductivity in argyrodite Ag_8SnSe_6. *Nat. Mater.* **22**, 999–1006 (2023).
49. Y. M. Pushcharovskya, D. Y. Pushcharovsky, The middle mantle of the Earth. *Geotectonics* **42**, 1–7 (2008).
50. W. G. Ernst, Earth's thermal evolution, mantle convection, and Hadean onset of plate tectonics. *J. Asian Earth Sci.* **135**, 334–348 (2017).
51. Y. Zhang, T. Sekine, J.-F. Lin, H. He, F. Liu, M. Zhang, T. Sato, W. Zhu, Y. Yu, Shock compression and melting of an Fe-Ni-Si Alloy: Implications for the temperature profile of the Earth's core and the heat flux across the core-mantle boundary. *J. Geophys. Res. Solid Earth* **123**, 1314–1327 (2018).
52. A. B. Belonoshko, Molecular dynamics of $MgSiO_3$ perovskite at high pressures: Equation of state, structure, and melting transition. *Geochim. Cosmochim. Acta* **58**, 4039–4047 (1994).
53. J.-F. Lin, E. Gregoryanz, V. V. Struzhkin, M. Somayazulu, H. Mao, R. J. Hemley, Melting behavior of H_2O at high pressures and temperatures. *Geophys. Res. Lett.* **32**, L11306 (2005).
54. M. Matsui, G. D. Price, Simulation of the pre-melting behaviour of $MgSiO_3$ perovskite at high pressures and temperatures. *Nature* **351**, 735–737 (1991).
55. B. J. Giletti, The nature of oxygen transport within minerals in the presence of hydrothermal water and the role of diffusion. *Chem. Geol.* **53**, 197–206 (1985).
56. S. M. Fortier, B. J. Giletti, An empirical model for predicting diffusion coefficients in silicate minerals. *Science* **245**, 1481–1484 (1989).
57. E. B. Watson, E. F. Baxter, Diffusion in solid-Earth systems. *Earth Planet. Sci. Lett.* **253**, 307–327 (2007).
58. J. R. Farver, Oxygen and hydrogen diffusion in minerals. *Rev. Mineral. Geochem.* **72**, 447–507 (2010).
59. B. Zhang, X. Wu, R. Zhou, Calculation of oxygen self-diffusion coefficients in Mg_2SiO_4 polymorphs and $MgSiO_3$ perovskite based on the compensation law. *Solid State Ion.* **186**, 20–28 (2011).
60. A. P. Ramirez, Colossal magnetoresistance. *J. Phys. Condens. Matter* **9**, 8171–8199 (1997).
61. P. W. Majewski, M. Gopinadhan, W.-S. Jang, J. L. Lutkenhaus, C. O. Osuji, Anisotropic ionic conductivity in block copolymer membranes by magnetic field alignment. *J. Am. Chem. Soc.* **132**, 17516–17522 (2010).
62. B. Wood, M. Walter, J. Wade, Accretion of the Earth and segregation of its core. *Nature* **441**, 825–833 (2006).
63. U. W. Bläß, F. Langenhorst, T. Boffa-Ballaran, F. Seifert, D. J. Frost, C. A. McCammon, A new oxygen-deficient perovskite phase $Ca(Fe_{0.4}Si_{0.6})O_{2.8}$ and phase relations along the join $CaSiO_3$–$CaFeO_{2.5}$ at transition zone conditions. *Phys. Chem. Minerals* **31**, 52–65 (2004).
64. U. W. Bläß, F. Langenhorst, D. J. Frost, F. Seifert, Oxygen deficient perovskites in the system $CaSiO_3$–$CaAlO_{2.5}$ and implications for the Earth's interior. *Phys. Chem. Minerals* **34**, 363–376 (2007).
65. M. Kanzaki, X. Xue, Y. Wu, S. Nie, Crystal structures of two oxygen-deficient perovskite phases in the $CaSiO_3$–$CaAlO_{2.5}$ join. *Phys. Chem. Minerals.* **44**, 717–733 (2017).
66. X. Li, R. Jeanloz, Laboratory studies of the electrical conductivity of silicate perovskites at high pressures and temperatures. *J. Geophys. Res. Solid Earth* **95**, 5067–5078 (1990).
67. A. Kavner, X. Li, R. Jeanloz, Electrical conductivity of a natural $(Mg,Fe)SiO_3$ majorite garnet. *Geophys. Res. Lett.* **22**, 3103–3106 (1995).
68. T. Yoshino, K. Kamada, C. Zhao, E. Ohtani, N. Hirao, Electrical conductivity model of Al-bearing bridgmanite with implications for the electrical structure of the Earth's lower mantle. *Earth Planet. Sci. Lett.* **434**, 208–219 (2016).
69. H. Fei, R. Huang, X. Yang, $CaSiO_3$ perovskite may cause electrical conductivity jump in the topmost lower mantle. *Geophys. Res. Lett.* **44**, 10226–10232 (2017).
70. L. Stixrude, R. Scipioni, M. P. Desjarlais, A silicate dynamo in the early Earth. *Nat. Commun.* **11**, 935 (2020).
71. K. Armstrong, D. J. Frost, C. A. McCammon, D. C. Rubie, T. B. Ballaran, Deep magma ocean formation set the oxidation state of Earth's mantle. *Science* **365**, 903–906 (2019).
72. H. Kuwahara, R. Nakada, S. Kadoya, T. Yoshino, T. Irifune, Hadean mantle oxidation inferred from melting of peridotite under lower-mantle conditions. *Nat. Geosci.* **16**, 461–465 (2023).
73. Q. Hu, D. Y. Kim, W. Yang, L. Yang, Y. Meng, L. Zhang, H.-K. Mao, FeO_2 and FeOOH under deep lower-mantle conditions and Earth's oxygen–hydrogen cycles. *Nature* **534**, 241–244 (2016).
74. J. Liu, Q. Hu, D. Y. Kim, Z. Wu, W. Wang, Y. Xiao, P. Chow, Y. Meng, V. B. Prakapenka, H.-K. Mao, W. L. Mao, Hydrogen-bearing iron peroxide and the origin of ultralow-velocity zones. *Nature* **551**, 494–497 (2017).
75. H.-K. Mao, W. L. Mao, Key problems of the four-dimensional Earth system. *Matter Radiat. Extremes* **5**, 038102 (2020).
76. G. Kresse, J. Furthmüller, Efficient iterative schemes for ab initio total-energy calculations using a plane-wave basis set. *Phys. Rev. B* **54**, 11169–11186 (1996).
77. D. Joubert, From ultrasoft pseudopotentials to the projector augmented-wave method. *Phys. Rev. B* **59**, 1758–1775 (1999).
78. J. P. Perdew, K. Burke, M. Ernzerhof, Generalized gradient approximation made simple. *Phys. Rev. Lett.* **77**, 3865–3868 (1996).
79. H. J. Monkhorst, J. D. Pack, Special points for brillouin-zone integrations. *Phys. Rev. B* **13**, 5188–5192 (1976).
80. W. G. Hoover, A. J. C. Ladd, B. Moran, High-strain-rate plastic flow studied via nonequilibrium molecular dynamics. *Phys. Rev. Lett.* **48**, 1818–1820 (1982).
81. L. Zhang, J. Han, H. Wang, R. Car, W. E, Deep potential molecular dynamics: A scalable model with the accuracy of quantum mechanics. *Phys. Rev. Lett.* **120**, 143001 (2018).
82. H. Wang, L. Zhang, J. Han, W. E, DeePMD-kit: A deep learning package for many-body potential energy representation and molecular dynamics. *Comput. Phys. Commun.* **228**, 178–184 (2018).
83. S. Plimpton, Fast parallel algorithms for short-range molecular dynamics. *J. Comput. Phys.* **117**, 1–19 (1995).

Acknowledgments: We thank A. B. Belonoshko for the fruitful discussions. **Funding:** This work was supported by the National Natural Science Foundation of China (to Z.W., grant number 42150101; to D.Y.K., grant number 11774015; to H.-k.M., grant number U2230401). D.Y.K. also acknowledges the support from Shanghai Science and Technology Committee, China (grant number 22JC1410300) and Shanghai Key Laboratory of Material Frontiers Research in Extreme Environments, China (grant number 22dz2260800). **Author contributions:** Conceptualization: Z.W., D.Y.K., and H.-k.M. Methodology: Z.W., Y.H., and D.Y.K. Investigation: Z.W., Y.H., D.Y.K., and H.-k.M. Data curation: Z.W. and D.Y.K. Formal analysis: Z.W. and D.Y.K. Visualization: Z.W. Software: Z.W. Validation: Z.W., D.Y.K., and H.-k.M. Resources: D.Y.K., H.-k.M., and Z.W. Supervision: H. M. and D.Y.K. Writing—original draft: Z.W. and D.Y.K. Writing—review and editing: Z.W., Y.H., D.Y.K., and H.-k.M. Funding acquisition: D.Y.K. and H.-k.M. Project administration: D.Y.K. and H.-k.M. **Competing interests:** The authors declare that they have no competing interests. **Data and materials availability:** All data needed to evaluate the conclusions in the paper are present in the paper and/or the Supplementary Materials.

Submitted 23 November 2024
Accepted 25 April 2025
Published 30 May 2025
10.1126/sciadv.adu8401